CALCULATION OF TRANSONIC VISCOUS FLOW AROUND A DELTA WING

Seppo Laine, Timo Siikonen and Petri Kaurinkoski

Laboratory of Aerodynamics
Helsinki University of Technology
02150 Espoo, Finland

ABSTRACT

Transonic viscous flow past a round leading edge cropped delta wing is determined by solving the Reynolds averaged thin-layer Navier–Stokes equations. Three algebraic turbulence models are used and laminar flow is also calculated. In the calculations the angle of attack varies between 10 and 40 degrees. The Mach number is 0.85 and the Reynolds number based on the root chord is $2.38 \cdot 10^6$. The results are compared with experiments.

INTRODUCTION

Computational fluid dynamics has reached a level where complicated, viscous flows can be simulated by numerically solving the Navier–Stokes equations. This has focused interest on cases that cannot be treated with simpler approximate methods. Vortical flows with shock waves and the interaction between shocks and boundary layer flows are cases that should be calculated using the Navier–Stokes equations. In the experiments it is often difficult to resolve the smallest details of the flowfield even though they may be important for the understanding of the overall behaviour of the flow. Computational methods provide a way to study the details of the flowfield.

The objective of the present study is to determine the flow past a cropped delta wing at transonic speed. The round leading edge delta wing with a leading edge sweep angle of 65° was examined in the International Vortex Flow Experiment on Euler Code Validation[1]. The same wing has been calculated using Euler and laminar Navier–Stokes codes[2,3,4]. The results of these calculations were promising, although they could not produce all the details correctly. Recently, Hilgenstock[5] has presented results from turbulent simulations.

The basic structure of the vortical flow past a delta wing at high angle of attack is shown in Fig. 1. This flow case is very challenging since the vortical flowfield with shock waves includes many complex fluid dynamic phenomena.

The Reynolds number of the calculated cases is $2.38 \cdot 10^6$, and therefore the calculations are performed with both totally laminar and totally turbulent boundary layer. The effects of turbulence are evaluated with either the Baldwin–Lomax turbulence model[6], the Degani–Schiff modified[7] version of the Baldwin–Lomax model or the Cebeci–Smith turbulence model[8]. The purpose in using several models as well as the laminar boundary layer assumption is to investigate the effects of the boundary layer type on the whole solution and to compare the behaviour of different algebraic turbulence models in a complex case. In this study emphasis is laid on resolving the flow details, although the integrated values of lift, drag and pitching moment are also given. The angle of attack varies between 10° and 40°, but detailed results are presented only for the case $\alpha = 10.38°$.

The calculations are performed with a computer code called FINFLO that solves the Reynolds averaged thin-layer Navier–Stokes equations with a finite-volume method. The equations are solved by an LU-factored implicit time integration method. The scheme is cell-centred and applies the flux-difference splitting of Roe[9]. The code utilizes a multigrid V-cycle for the acceleration of convergence and is able to handle multiblock grids. The code has been developed at the Laboratory of Aerodynamics of Helsinki University of Technology[10,11].
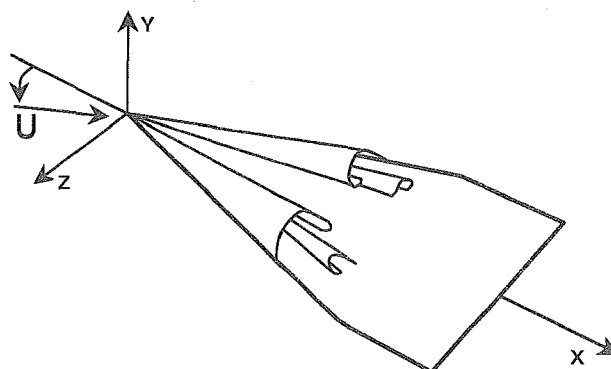

Fig.1 The structure of the flowfield near a delta wing with primary and secondary vortices.

NUMERICAL METHOD

Governing equations

The Navier–Stokes equations can be written in a conservative form using Cartesian coordinates as

$$\frac{\partial U}{\partial t} + \frac{\partial F(U)}{\partial x} + \frac{\partial G(U)}{\partial y} + \frac{\partial H(U)}{\partial z} = 0 \qquad (1)$$

where $U = (\rho \quad \rho u \quad \rho v \quad \rho w \quad e)^T$. In the present solution, a finite-volume technique is applied. The flow equations have an integral form

$$\frac{\partial}{\partial t} \int_V U \, dV + \int_S \vec{F}(U) \cdot d\vec{S} = 0 \qquad (2)$$

for an arbitrary fixed region V with a boundary S. Performing the integrations for a computational cell i yields

$$V_i \frac{dU_i}{dt} = \sum_{faces} -S\hat{F} \qquad (3)$$

where the sum is taken over the faces of the computational cell and

$$\hat{F} = n_x F + n_y G + n_z H \qquad (4)$$

Here $n_x \vec{i} + n_y \vec{j} + n_z \vec{k}$ is the unit normal vector of the cell face and F, G and H are the fluxes in the x-, y- and z-directions respectively.

Turbulence models. The effects of turbulence are taken into account by modifying the viscosity and heat transfer coefficients. The viscosity is replaced by $\mu + \mu_t$, and the thermal conductivity by

$$\frac{\mu}{Pr} + \frac{\mu_t}{Pr_t}$$

where μ_T is the turbulent viscosity and Pr_t is the turbulent Prandtl number. While in laminar regions the Prandtl number is assumed to have a constant value 0.72, another constant value of 0.9 is used for Pr_t. In the present calculations three different algebraic turbulence models have been applied: the Baldwin-Lomax model, the Degani–Schiff modified version of the Baldwin–Lomax model and the Cebeci-Smith model. The Baldwin–Lomax and the Cebeci–Smith models are suitable in their original form for boundary layer type flows. However, the flow on the leeside of the delta wing has a strong vortical structure. In the Baldwin-Lomax model the modification of Degani and Schiff[7] permits the model to differentiate between the vorticity within the attached boundary layers and the vorticity on the surfaces of the separation. Hence, the length scale is based on the thickness of the attached boundary layer rather than on the normal distance between the wing surface and the vortex core. In the Cebeci-Smith model a method proposed by Stock and Haase[8] is used, which, instead of requiring the boundary layer thickness, utilizes a special formula for the turbulence length scale.

Spatial discretization

The calculation of the fluxes is performed in two stages. The inviscid part of the flux on the cell surface is calculated by solving approximately a locally one-dimensional Riemann problem. The viscous part is centrally differenced and treated separately from the inviscid part. Since the thin-layer approximation has been adopted, only those viscous terms evaluated in the normal direction of the wall are retained.

For the calculation of the inviscid part of the flux, the rotational matrix T is utilized

$$\hat{F} = T^{-1}[F(TU)] \qquad (5)$$

where F has the same functional form as in Eq. (4)

The computer code includes two alternative ways to calculate F: the flux-difference splitting developed by Roe[9], and the flux-vector splitting method of van Leer[12]. In the present study, Roe's method has been used. In the calculation of the fluxes, either by Roe's or van Leer's method, the evaluation of the solution vector on both sides of the cell surface is performed with a MUSCL-type approach.

Boundary treatment. At the free-stream boundary the values of the dependent variables are kept as constants. In the calculation of the inviscid flux at the solid boundary the flux-splitting is not used. The only contribution to the momentum flux arises from the pressure terms. The wall pressure is evaluated using a second-order extrapolation from the interior cells. The viscous fluxes are evaluated by setting $u = v = w = 0$ at the wall.

Solution Algorithm

The discretized equations are integrated in time by applying the LU-factorization[11]. This is based on the approximate factorization and on the splitting of the Jacobians of the flux terms. The resulting implicit stage consists of a backward and forward sweep in every coordinate direction. In the integration a spatially varying time step is utilized. Since the Jacobian matrices are evaluated approximately, the time-step size is limited. With the present time integration scheme the limitation is more severe with van Leer's method than with Roe's method.

In order to accelerate the convergence, a multigrid cycling is used. The method of Jameson[13] with a simple V-cycle has been adopted. The spatial discretization applied on the coarse grid levels is of the first order, which allows the use of a larger CFL-number on those grid levels.

WING GEOMETRY AND COMPUTATIONAL GRID

The wing selected for these calculations is the round leading edge cropped delta wing used in the International Vortex Flow Experiment on Euler Code Validation[1]. The leading edge sweep angle is 65° and the wing has a taper ratio of 0.15. The reference length for the Reynolds number and moment coefficient is the root chord c_r. The wing profile is constant over the span and is defined at the root by

$$y = \begin{cases} \pm(0.1183\sqrt{x} - 0.2101x + 0.3501x^2 - 0.3406x^3) \\ \qquad\qquad\qquad\qquad\qquad\qquad 0 \le x \le 0.4 \\ \text{NACA 64A005} \\ \qquad\qquad\qquad\qquad\qquad\qquad 0.4 < x \le 1 \end{cases}$$

The grid used in the calculations is a single-block structured $128 \times 48 \times 64$ O–O grid. The outer edge of the grid with free-stream boundary conditions is a sphere centred at the middle of the root chord with a radius of $10c_r$. The number of cells in the near normal direction to the surface is 48. The grid is heavily clustered on the wing surface to obtain approximately 25 cells in the boundary layer. According to earlier experience this gives sufficient resolution to describe the boundary layer. The height of the cells on the surface is about $3 \cdot 10^{-5}$, resulting in a y^+ value of the order of 1 in the middle of the first cell. The grid is also slightly clustered on the leading edge and the trailing edge and also on the tip to obtain better resolution in areas of large gradients. The grid is nearly orthogonal near the wing surface except at the trailing edge and the tip. The grid is generated using a transfinite interpolation method. The wing surface is shown in Fig. 2 and the grid near the wing is presented in Fig. 3. Since only symmetric cases are calculated, only half of the wing is modelled.
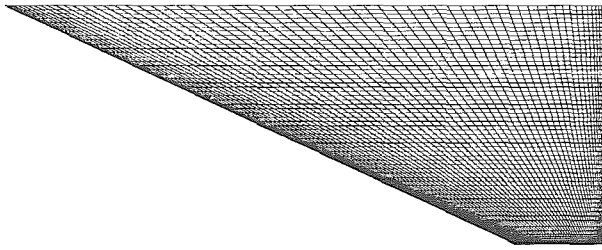
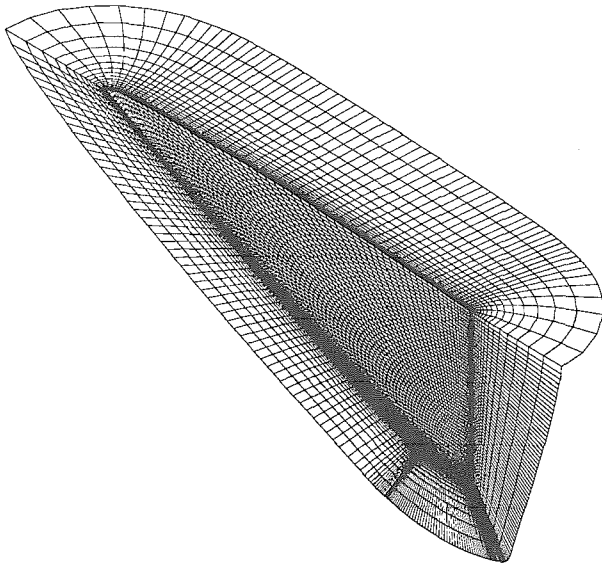**Fig.2** The grid on the surface of the cropped delta wing.

Fig.3 The grid near the cropped delta wing.

COMPUTATIONAL RESULTS

In all the calculated test cases the Mach number is 0.85 and the Reynolds number based on the root chord is $2.38 \cdot 10^6$. The angle of attack α is varied between 10 degrees and 40 degrees. Two different cases are studied: laminar flow and turbulent flow. The turbulent viscosity is evaluated using either the Baldwin-Lomax turbulence model, the Degani–Schiff modified version of the Baldwin–Lomax model or the Cebeci–Smith turbulence model. In the calculations five multigrid levels are used, which results in a tenfold increase in the convergence speed. At moderate angles of attack about 200–300 iteration cycles are required to obtain a sufficiently converged solution. This is equal to 1.5–2.5 hours of CPU time on a Cray X-MP computer. The van Albada flux-limiter was used in the chordwise direction to obtain non-oscillatory results near shock waves. Typical convergence histories for C_L are presented in Fig. 4.

Test Case $\alpha = 10.38°$

The calculated pressure coefficient distributions on the upper surface for inviscid, laminar and turbulent cases are compared with experimental results[1] in Fig. 5 at $x/c_r = 0.3$, 0.6, and 0.8. As can be seen, the laminar flow calculations agree better with the experiments than

do the turbulent or the inviscid calculations, especially at $x/c_r = 0.3$ and 0.6. Near the trailing edge, however, at $x/c_r = 0.8$ the turbulent solution is better than the laminar solution, except near the suction peak. Thus it can be assumed that the boundary layer in the experiments was laminar at $x/c_r = 0.3$ and $x/c_r = 0.6$, whereas it was turbulent at $x/c_r = 0.8$. The computational results reveal a weak shock wave originating from the wing root at $x/c_r \approx 0.6$. It is evident that at least this shock wave induces the boundary layer transition from laminar to turbulent.
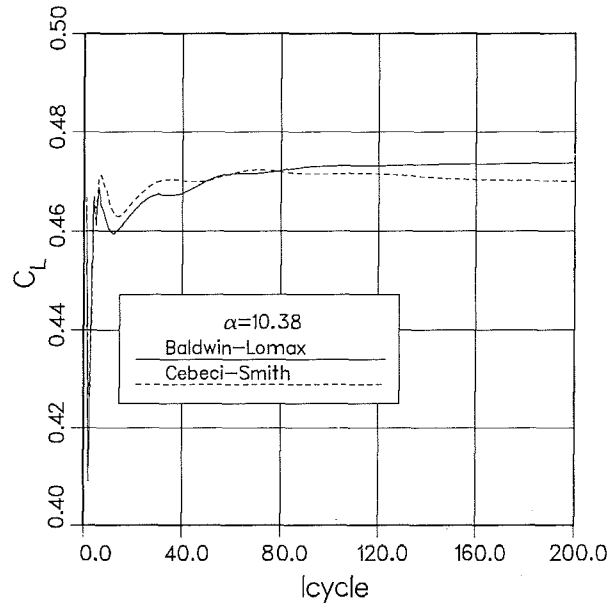

Fig.4 The convergence history of C_L at $\alpha = 10.38°$ using the Baldwin–Lomax and the Cebeci–Smith turbulence models.

Figs. 6a–d show the oil flow plots for different cases at $\alpha = 10.38°$ and Figs. 7a–d present the corresponding C_p-distributions on the upper surface. The total pressure contours for different solutions at different cross sections are presented in Figs. 8–11.

Laminar flow. The results of the laminar case show two suction peaks and two local pressure maximums at $x/c_r = 0.3$. In principle the suction peaks correspond to separation lines and the pressure maximums correspond to reattachment lines. These results — together with the oil flow plot in Fig. 6a revealing two reattachment lines at $x/c_r = 0.3$ — indicate that at this section there are two vorticies. The locations of the centres of these vorticies can be determined from Fig. 8a, which presents the total pressure contours. The centre of the primary vortex lies at $\eta = 0.75$, while the secondary vortex centre, which is not clearly visible, lies at $\eta = 0.81$.

At $x/c_r = 0.6$ there are three clearly visible suction peaks in Fig. 5 at $\eta = 0.71$, $\eta = 0.81$ and $\eta = 1.0$. In addition there is a very weak local pressure minimum at $\eta = 0.9$. This is consistent with the oil flow plot, which shows three separation lines. The weak pressure minimum indicates the development of a fourth vortex which, however, is still too weak to become a clear vortex. The oil flow plot in Fig. 6a and total pressure plot in Fig. 8b confirm these conclusions.

At $x/c_r = 0.8$ three suction peaks are seen in Fig.5 at $\eta = 0.71$, $\eta = 0.83$ and $\eta = 1.0$. There is also a very weak local minimum at $\eta = 0.90$. The total pressure plot in Fig. 8c reveals four vorticies, the fourth of which is centred at $\eta \approx 0.94$. This vortex is weak and according to the oil flow plot it vanishes at $x/c_r \approx 0.85$.

The oil flow plot in Fig. 6a confirms these conclusions, revealing the three clear separation lines and the weak one near the tip. The reattachment lines are also visible, although their locations can not be determined as accurately as the location of the separation lines. Near the root at $x/c_r \approx 0.7$ there is an area of separating flow. This is evidently shock-induced separation which is not found from the results of turbulent calculations.

The computed skin friction coefficient distributions give further information about the boundary layer behaviour on the surface. The skin friction x- and z-components nondimensionalized with the free-stream kinetic pressure are presented in Fig. 12 at spanwise section $2z/b = 0.57$.

Turbulent flow. At $x/c_r = 0.3$ the turbulent calculations cannot properly describe the vortical flow pattern. The pressure distribution near the root is relatively good with all the applied turbulence models, but they all fail to accurately predict the leading edge separation. Therefore the suction peak is located too close to the leading edge and is far too strong.

At $x/c_r = 0.6$ the turbulent solutions capture a clear primary vortex, the centre of which lies at $\eta = 0.78$, although differences are found concerning the existence of a secondary vortex. The Baldwin–Lomax model shows only a primary vortex, while the Cebeci–Smith model reveals a starting and the Degani–Shiff model gives a clear secondary vortex. They all overpredict the strength of the suction peak, and the Baldwin–Lomax model gives no distinct pressure maximum for the reattachment. Overall the turbulent solutions are qualitatively good, but there are quantitative errors in the details.

At $x/c_r = 0.8$ all the turbulent calculations yield an excellent pressure distribution near the root, but the strength of the suction peak is overestimated. The Baldwin–Lomax model captures only one large vortex, while the Cebeci–Smith model also locates a secondary vortex. The Degani–Shiff model even finds a distinct tertiary vortex which, however, is quite weak. In all cases, the centre of the primary vortex lies at $\eta = 0.78$.

The differences between the results obtained with different turbulence models can partly be explained by the differences in the models. The Baldwin–Lomax model tends to considerably overpredict the turbulent viscosity in areas of vortical flow. This characteristic was eliminated by the implementation of the Degani–Schiff modification to the Baldwin–Lomax turbulence model. The Cebeci–Smith model is applied with the modification proposed by Stock and Haase. This model does not seem to be disturbed by the presence of a large vortex, and the turbulent viscosities so obtained are smaller than those obtained from the

Baldwin–Lomax model, although still clearly larger than those of the Degani–Schiff model. The overpredicted turbulent viscosity of the Baldwin–Lomax model hinders the development of a secondary vortex. Both the Cebeci–Smith model and the Degani–Schiff model allow the development of multiple vorticies.

The qualitative differences in these results are clearly seen from the oil flow plots in Figs. 6a–d. The shock-induced separation found from laminar solution in the root area is not present in any of the turbulent solutions. Most probably the primary separation in the tests was laminar, although the reattached flow was turbulent as was the flow on the upper surface downstream from the midchord near the wing root.

Test Case $\alpha = 20.82°$

This case, which is the angle of attack for maximum lift, is calculated with both laminar and turbulent boundary layer. The laminar results suggest that the wing has already stalled. The turbulent calculations with the Cebeci–Smith model result in a slightly stalled wing, yielding lift and drag coefficients a little too small in comparison with the experimental results.

Laminar flow. The laminar solution suggests that vortex bursting due to a shock wave occurs at $x/c_r \approx 0.4$. The intensity of the vortex decreases rapidly after that point and the whole flow pattern is destroyed. This can be seen from the oil flow plot in Fig. 13a. The accuracy of the predicted pressure distribution at $x/c_r = 0.3$ is passable in comparison with the experimental results. After the vortex bursting the pressure is essentially constant, which is a typical feature of separated flow.

Turbulent flow. In the solution with the Cebeci–Smith turbulence model, vortex bursting occurred at $x/c_r \approx 0.7$. Before that point, at $x/c_r = 0.3$ and at $x/c_r = 0.6$, the pressure distributions are relatively close to the experimental results. At $x/c_r = 0.8$ the vortex bursting has suppressed the flow details and therefore the pressure distribution is clearly in error. It should be noted that in the experiments the suction peak at $x/c_r = 0.8$ had become distinctly weaker in comparison with that of $x/c_r = 0.6$. This is a sign of an approaching vortex bursting. The oil flow plot of this result is shown in Fig. 13b.

Lift, drag and pitching moment

The coefficients of lift, drag and pitching moment at several angles of attack are presented in Figs. 15 and 16 and in Tables 1 and 2. They also include the corresponding experimental results[14]. The moment coefficient is defined as positive when it tends to increase the angle of attack and it is calculated around the point $x/c_r = 0.57$.

The calculated aerodynamic coefficients agree quite well with the experimental values as long as the wing is not stalled. Vortex bursting starts too early in the calculations and therefore the stalling is not accurately predicted. The results for $\alpha = 10.38°$ show that the Cebeci–Smith and the

Degani–Schiff turbulence models produce the best results. At $\alpha = 20.82°$ only the Cebeci–Smith model gives results that are comparable with the experiments.

Table 1 The lift, drag and pitching moment coefficients at $\alpha = 10.38°$, $Ma = 0.85$ and $Re = 2.38 \cdot 10^6$ with various boundary layer types.

$\alpha = 10.38°$, $Re = 2.38 \cdot 10^6$, $Ma = 0.85$			
Test Case	C_L	C_D	$C_{m.57}$
Laminar	0.4798	0.0795	-0.0117
Baldwin–Lomax	0.4737	0.0811	-0.0123
Degani–Schiff	0.4659	0.0794	-0.0095
Cebeci–Smith	0.4696	0.0804	-0.0103
Experiments	0.4467	0.0805	-0.0082

Table 2 The lift, drag and pitching moment coefficients at $\alpha = 20.82°$, $Ma = 0.85$ and $Re = 2.38 \cdot 10^6$ with various boundary layer types.

$\alpha = 20.82°$, $Re = 2.38 \cdot 10^6$, $Ma = 0.85$			
Test Case	C_L	C_D	$C_{m.57}$
Laminar	0.7086	0.2658	-0.0256
Degani–Schiff	0.7107	0.2685	-0.0196
Cebeci–Smith	0.8594	0.3157	-0.0147
Experiments	0.9515	0.3521	-0.0283

CONCLUSIONS

Transonic viscous flow around a round leading edge cropped delta wing has been calculated at $Ma = 0.85$ and $Re = 2.38 \cdot 10^6$. Both laminar and turbulent boundary layer assumptions have been used applying three different algebraic turbulence models. The basic features of the flow are resolved and up to four vortices can be found from the solutions. The details are dependent on the turbulence modelling applied.

At $\alpha = 10.38°$ downstream from the wing apex to the middle of the wing the the laminar solution is closer to the experimental results than are the turbulent solutions, but towards the trailing edge the turbulent solutions agree better with the experiments. The computed lift, drag and pitching moment values agree quite well with the experimental values.

At $\alpha = 20.38°$, which is just below the stalling in the experiments, the calculations show vortex breakdown too early, and as a result the calculated lift and drag coefficients are too small. Only the results of the Cebeci–Smith model are comparable with the experiments.

Of the three turbulence models, the original Baldwin–Lomax gave the poorest results, presumably because of its excessively high turbulent viscosity. The two other models, the Cebeci–Smith model and the modified Baldwin–Lomax model, yield comparable results at $\alpha = 10.38°$.

REFERENCES

1. Proceedings of the Symposium on International Vortex Flow Experiment on Euler Code Validation, Edited by A. Elsenaar and G. Eriksson, Stockholm, Sweden, Oct, 1986.

2. Rizzi, A. and Müller, B., Large-Scale Simulation of Laminar Vortex Flow Over Delta Wing, AIAA Journal, Vol. 27, No. 7, 1989.

3. Müller, B. and Rizzi, A., Navier-Stokes Computation of Transonic Vortices Over a Round Leading Edge Delta Wing, International Journal for Numerical Methods in Fluids, Vol. 9, 1989.

4. Kumar, A. and Das, A., Computation of Vortex Flow on a Delta Wing at Transonic Speed. In Symposium Transonicum III in Göttingen 1988, Ed. J. Zierep and H. Oertel, Springer Verlag, 1989.

5. Hilgenstock, A., Validation of Transonic Turbulent Flows Past Delta Wing Configurations, Aeronautical Journal, Aug/Sept, 1991.

6. Baldwin, B.S., Lomax, H., Thin Layer Approximation and Algebraic Model for Separated Turbulent Flows, AIAA Paper 78-257, Jan., 1978.

7. Degani, D., Schiff, L.B., Computation of Turbulent Supersonic Flows around Pointed Bodies Having Crossflow Separation, J. Comput. Phys., Vol. 66, No. 1, 1986.

8. Stock, H.W., Haase, W., Determination of Length Scales in Algebraic Turbulence Models for Navier-Stokes Methods, AIAA Journal, Vol. 27, No. 1, 1989.

9. Roe, P.L., Approximate Riemann Solvers, Parameter Vectors, and Difference Schemes, Journal of Computational Physics, Vol. 43, 1981.

10. Siikonen, T., A Three-Dimensional Multigrid Algorithm for the Euler and the Thin-Layer Navier–Stokes Equations, Helsinki University of Technology, Laboratory of Aerodynamics, Report No. A-12, 1991.

11. Siikonen, T., Hoffren, J. and Laine, S., A Multigrid LU Factorization Scheme for the Thin-Layer Navier–Stokes Equations, 17th ICAS Congress, Stockholm, 1990.

12. van Leer, B., Flux-Vector Splitting for the Euler Equations, Proc. 8th Int. Conf. on Numerical Methods in Fluid Dynamics, Aachen, 1982 (also Lecture Notes in Physics, Vol. 170, 1982).

13. Jameson, A., Yoon, S., Multigrid Solution of the Euler Equations Using Implicit Schemes, AIAA Journal, Vol. 24, No.11, 1986.

14. Hartmann, K., US/European Transonic Vortex Flow Experiment — Data Lists of Force Measurements, DFVLR, IB 222 – 86 A 03, Göttingen, 1986.
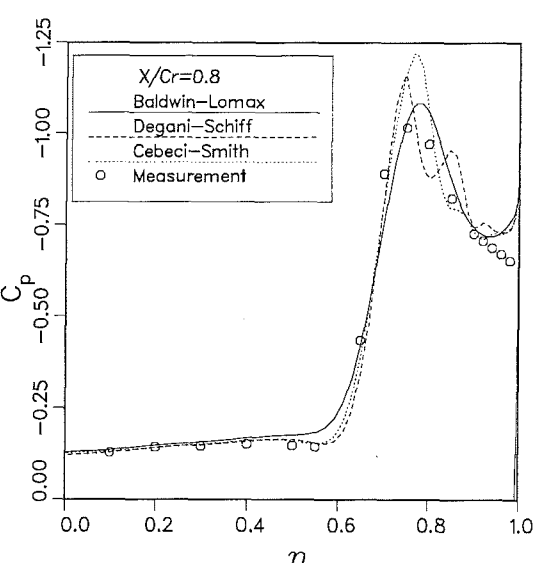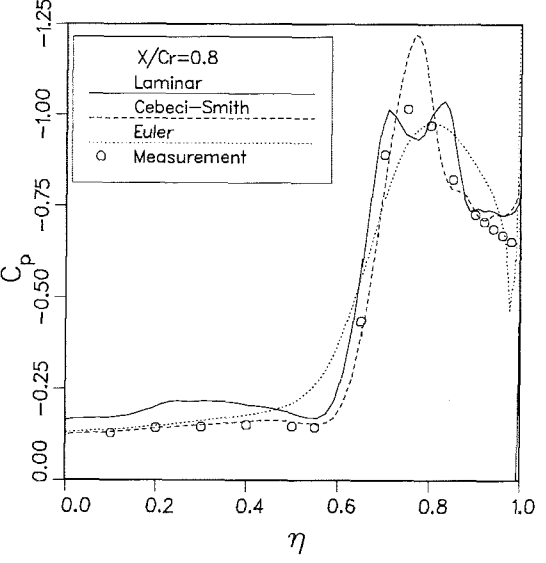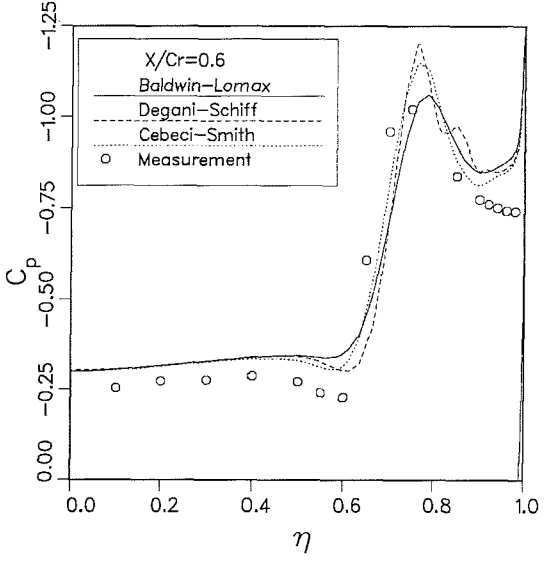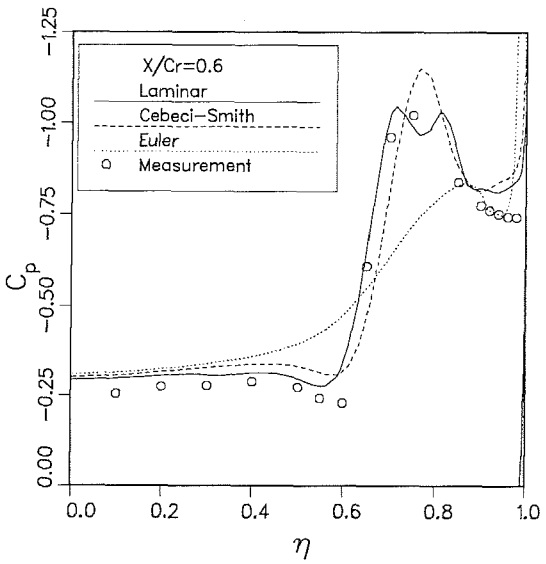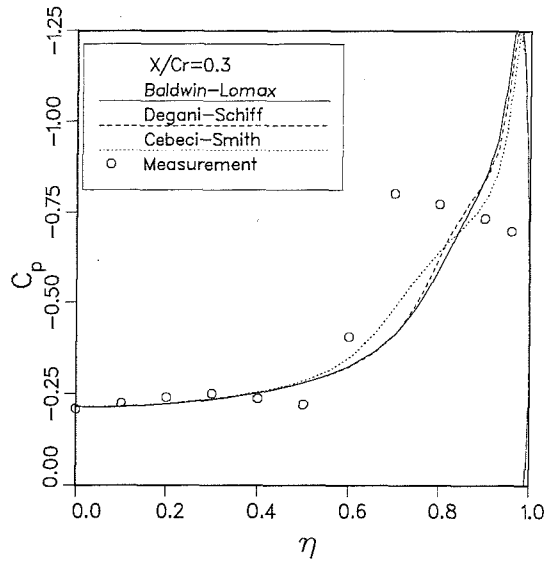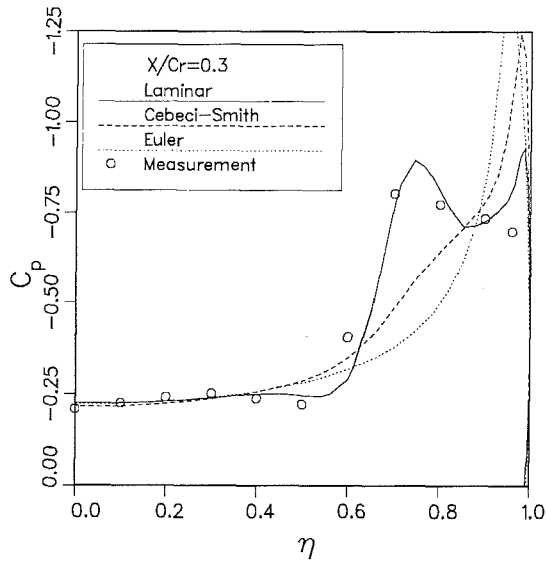
Fig.5 a. C_p-distributions at $x/c_r = 0.3, 0.6$ and 0.8 for $\alpha = 10.38°$ using laminar boundary layer, the Cebeci–Smith model and inviscid flow.

Fig.5 b C_p-distributions at $x/c_r = 0.3, 0.6$ and 0.8 for $\alpha = 10.38°$ using the Baldwin–Lomax, the Degani–Schiff and the Cebeci–Smith model.

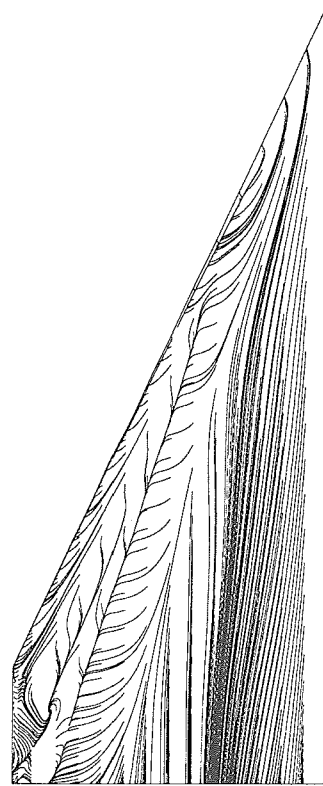**Fig.6 a.** Surface streamlines of $\alpha = 10.38°$ using laminar boundary layer.

Fig.6 c. Surface streamlines of $\alpha = 10.38°$ using the Degani–Schiff turbulence model.
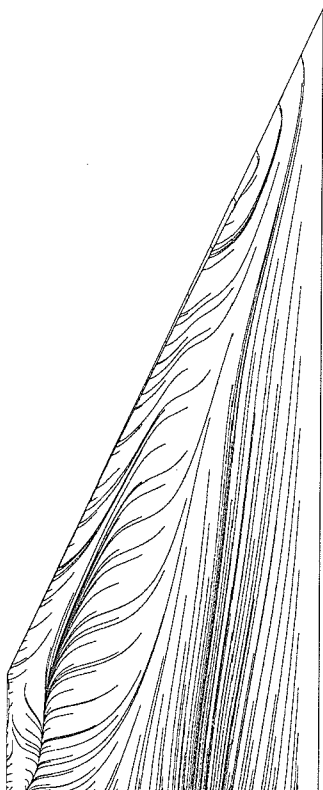
Fig.6 b. Surface streamlines of $\alpha = 10.38°$ using the Baldwin–Lomax turbulence model.
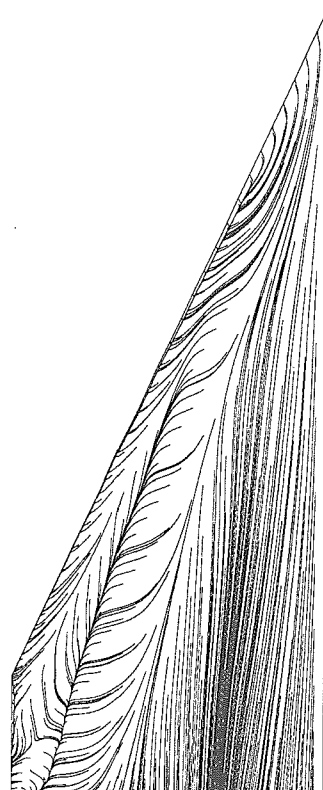
Fig.6 d. Surface streamlines of $\alpha = 10.38°$ using the Cebeci–Smith turbulence model.

291
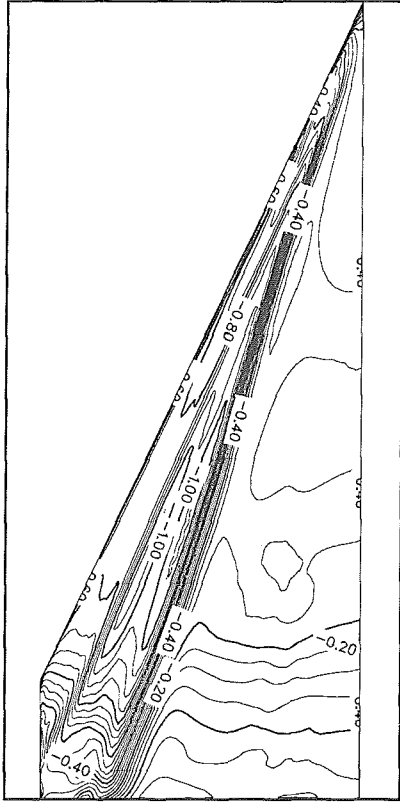
Fig.7 a. C_p-distribution at $\alpha = 10.38°$ using laminar boundary layer.
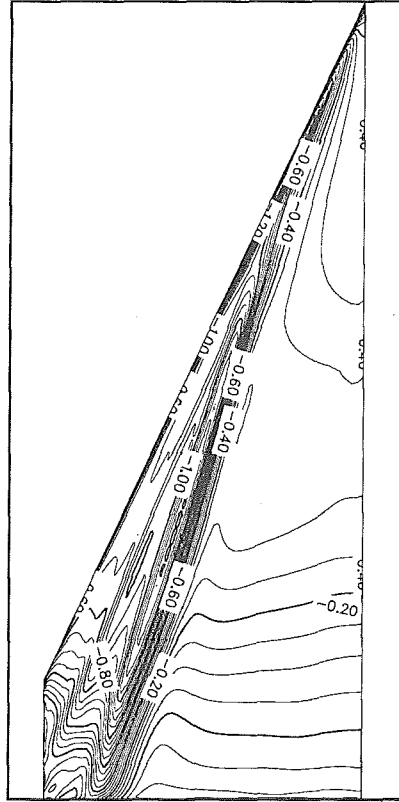
Fig.7 c. C_p-distribution at $\alpha = 10.38°$ using the Degani–Schiff turbulence model.
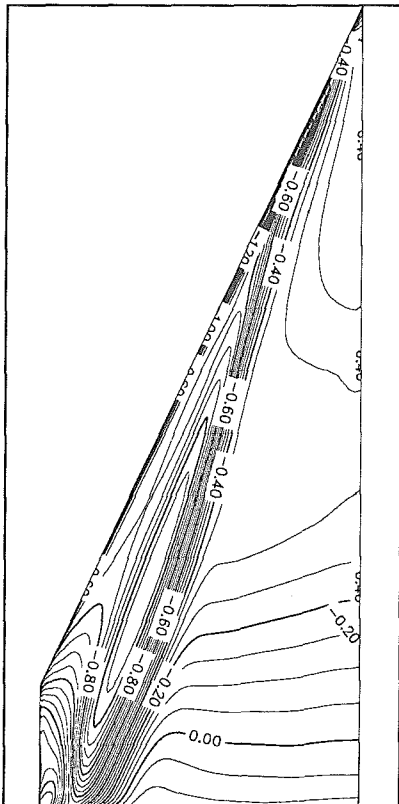
Fig.7 b. C_p-distribution at $\alpha = 10.38°$ using the Baldwin–Lomax turbulence model.
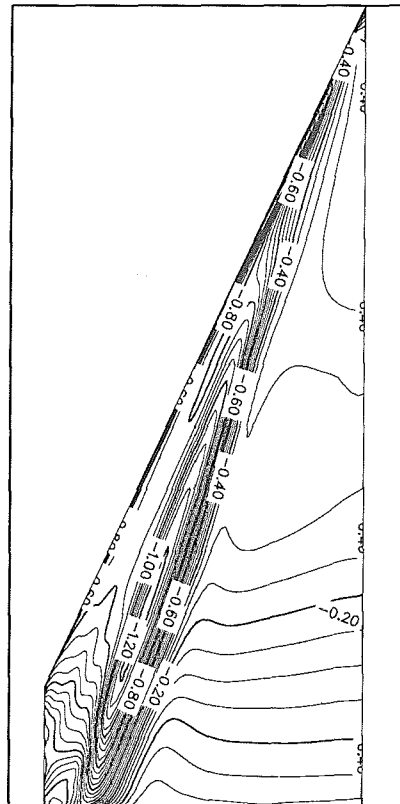
Fig.7 d. C_p-distribution at $\alpha = 10.38°$ using the Cebeci–Smith turbulence model.

292
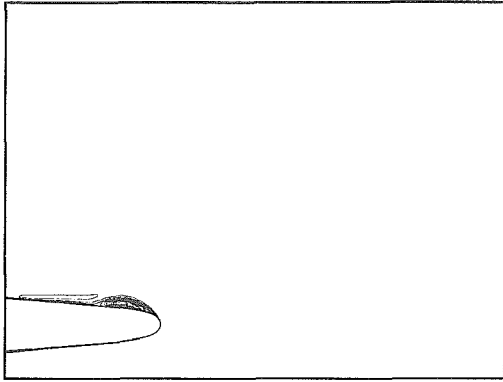
Fig.8 a. Total pressure contours at $x/c_r = 0.3$ for $\alpha = 10.38°$ using laminar boundary layer.
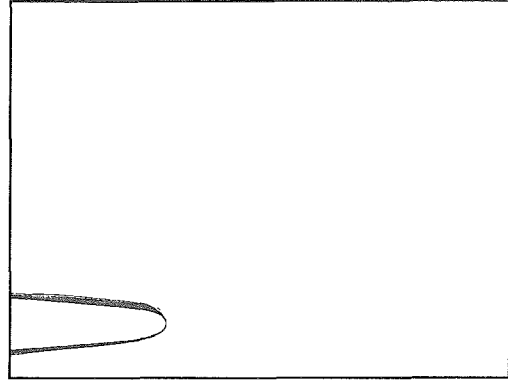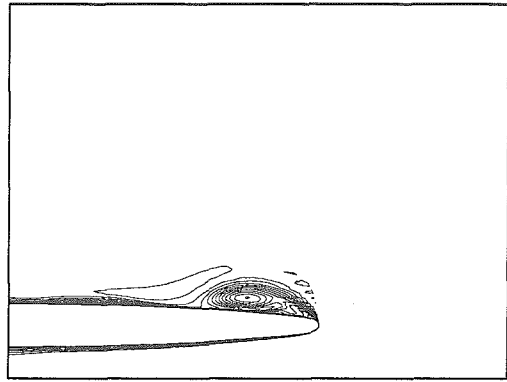

Fig.9 a. Total pressure contours at $x/c_r = 0.3$ for $\alpha = 10.38°$ using the Baldwin–Lomax model.
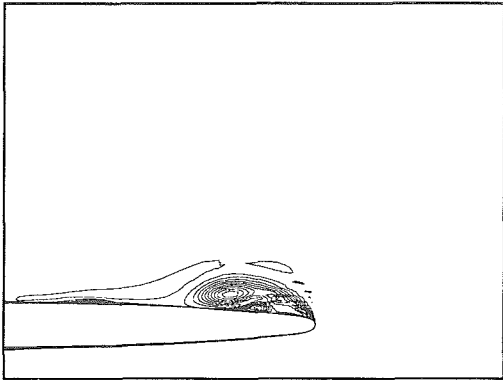
Fig.8 b. Total pressure contours at $x/c_r = 0.6$ for $\alpha = 10.38°$ using laminar boundary layer.
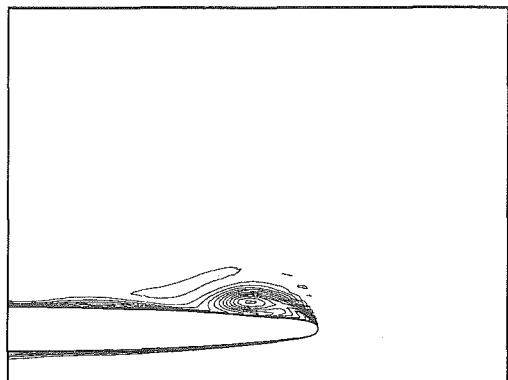
Fig.9 b. Total pressure contours at $x/c_r = 0.6$ for $\alpha = 10.38°$ using the Baldwin–Lomax model.
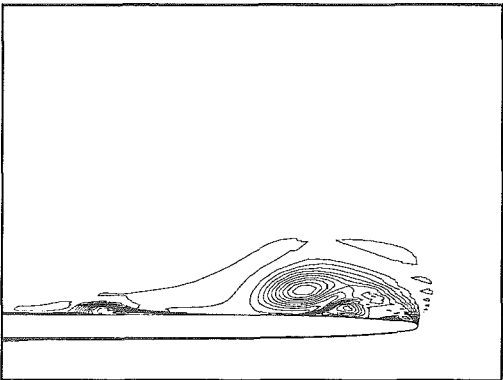
Fig.8 c. Total pressure contours at $x/c_r = 0.8$ for $\alpha = 10.38°$ using laminar boundary layer.
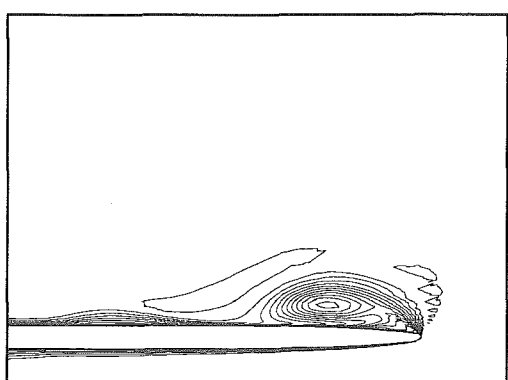
Fig.9 c. Total pressure contours at $x/c_r = 0.8$ for $\alpha = 10.38°$ using the Baldwin–Lomax model.

Fig.8 d. Total pressure contours at $x/c_r = 1.05$ for $\alpha = 10.38°$ using laminar boundary layer.
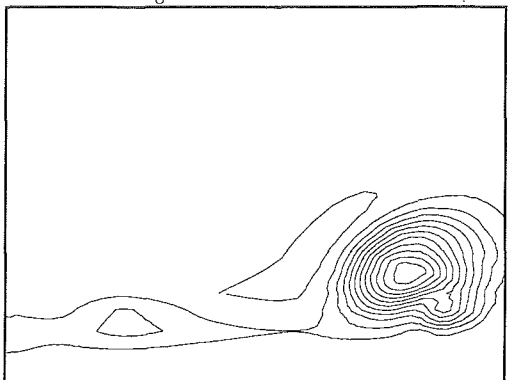
Fig.9 d. Total pressure contours at $x/c_r = 1.05$ for $\alpha = 10.38°$ using the Baldwin–Lomax model.
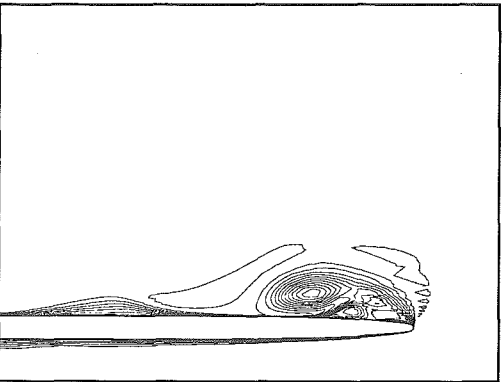
293
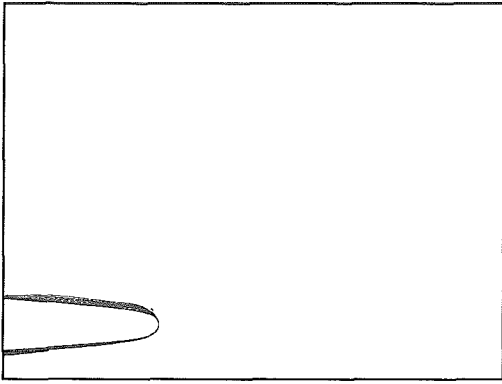
Fig.10 a. Total pressure contours at $x/c_r = 0.3$ for $\alpha = 10.38°$ using Degani–Schiff model.
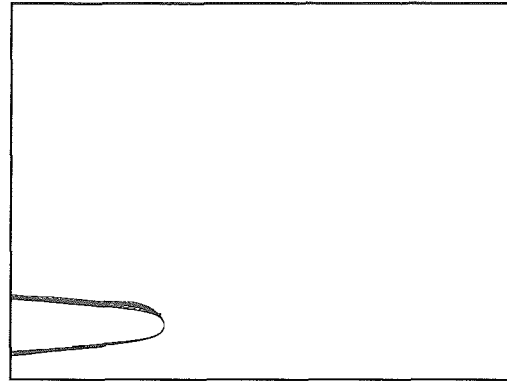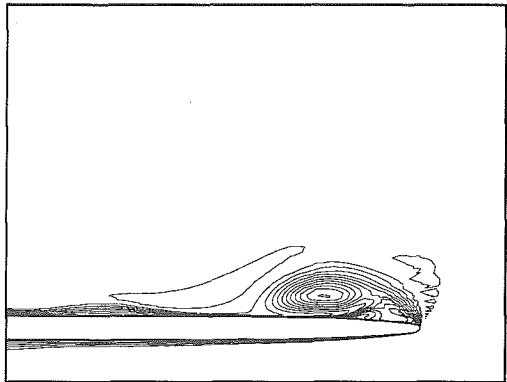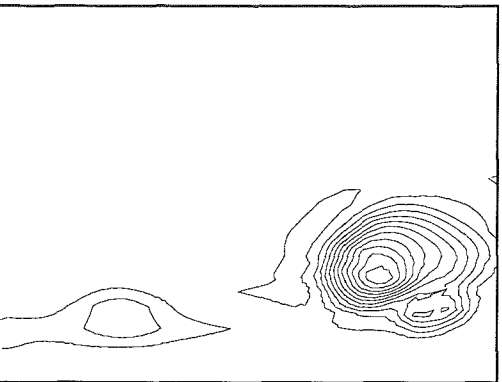

Fig.11 a. Total pressure contours at $x/c_r = 0.3$ for $\alpha = 10.38°$ using the Cebeci–Smith model.
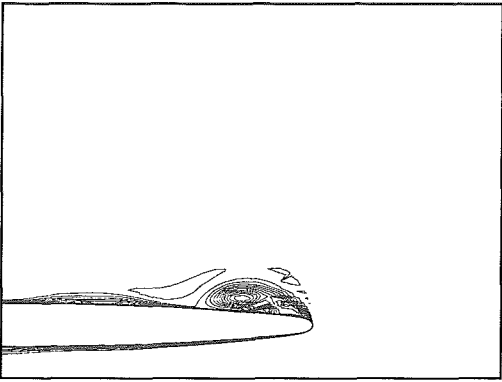
Fig.10 b. Total pressure contours at $x/c_r = 0.6$ for $\alpha = 10.38°$ using Degani–Schiff model.

Fig.11 b. Total pressure contours at $x/c_r = 0.6$ for $\alpha = 10.38°$ using the Cebeci–Smith model.

Fig.10 c. Total pressure contours at $x/c_r = 0.8$ for $\alpha = 10.38°$ using Degani–Schiff model.

Fig.11 c. Total pressure contours at $x/c_r = 0.8$ for $\alpha = 10.38°$ using the Cebeci–Smith model.

Fig.10 d. Total pressure contours at $x/c_r = 1.05$ for $\alpha = 10.38°$ using Degani–Schiff model.
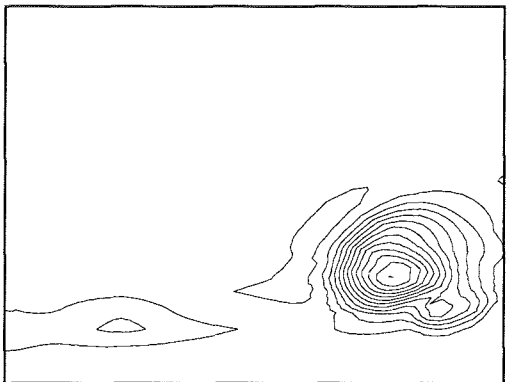

Fig.11 d. Total pressure contours at $x/c_r = 1.05$ for $\alpha = 10.38°$ using the Cebeci–Smith model.
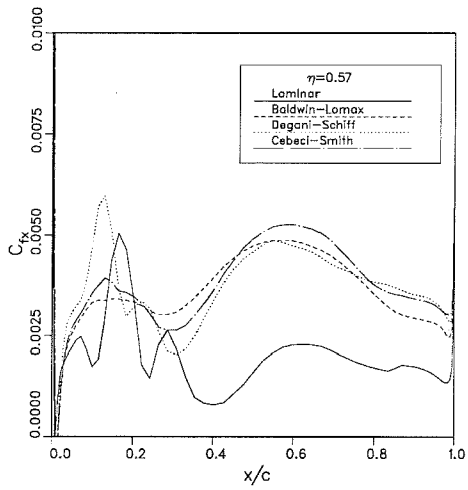
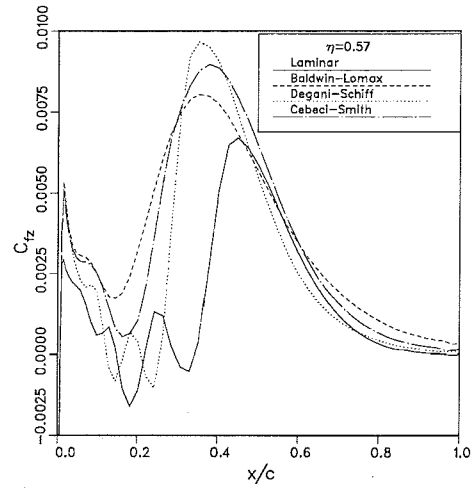**Fig.12 a.** C_{f_x}-distributions at section $2z/b = 0.57$.

Fig.12 a. C_{f_z}-distributions at section $2z/b = 0.57$.

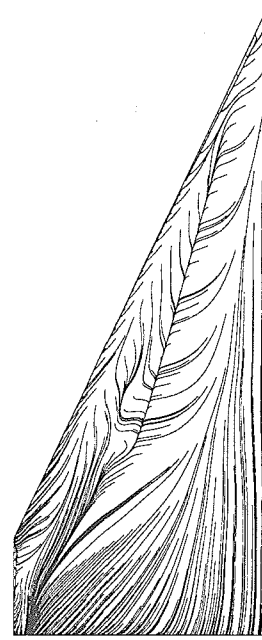**Fig.13 a.** Surface streamlines of $\alpha = 20.82°$ using laminar boundary layer.

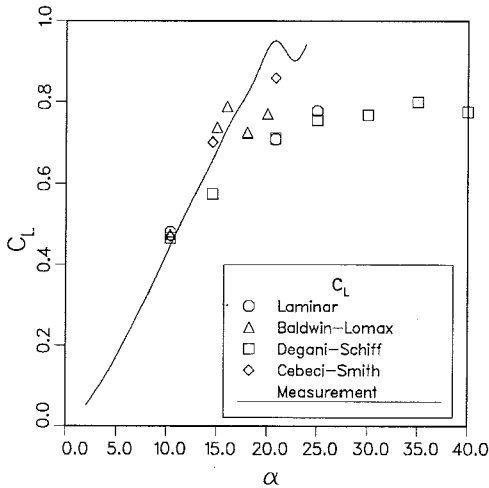**Fig.13 b.** Surface streamlines of $\alpha = 20.82°$ using Cebeci–Smith turbulence model.

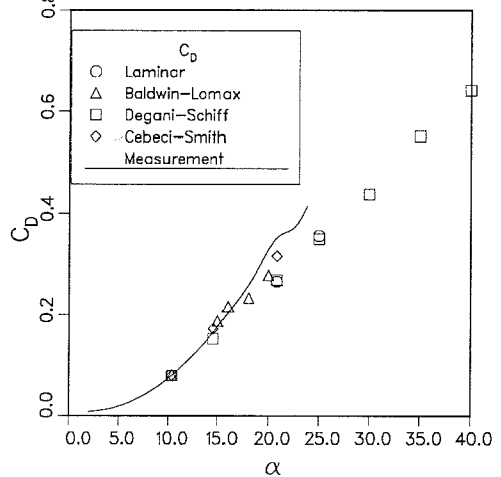**Fig.14 a.** C_L versus α for different solutions.

Fig.14 b. C_D versus α for different solutions.